Journal of Materials Chemistry A

RSC Publishing

PAPER

View Article Online
View Journal | View Issue

Cite this: J. Mater. Chem. A, 2013, 1, 9781

$BaNb_{0.05}Fe_{0.95}O_{3-\delta}$ as a new oxygen reduction electrocatalyst for intermediate temperature solid oxide fuel cells

Feifei Dong,[a] Yubo Chen,[a] Ran Ran,*[a] Dengjie Chen,[a] Moses O. Tadé,[b] Shaomin Liu[b] and Zongping Shao*[ab]

Received 11th April 2013
Accepted 3rd June 2013

DOI: 10.1039/c3ta11447c

www.rsc.org/MaterialsA

Cobalt-free perovskite $BaNb_{0.05}Fe_{0.95}O_{3-\delta}$ (BNF) is synthesized and characterized towards application as a cathode material for intermediate temperature solid oxide fuel cells. *In situ* X-ray diffraction and transmission electron microscopy are applied to study the crystal structure and thermally induced phase transformation. BNF exists as a multiphase structure composed of a monoclinic phase and a cubic phase at room temperature, and then undergoes a phase transformation to a cubic structure starting at ~400 °C, which is maintained at temperatures up to 900 °C during a thermal cycle between room temperature and 900 °C; while it retains the cubic perovskite lattice structure on cooling from 900 °C to room temperature. Oxygen temperature-programmed desorption, combined thermal expansion and thermo-gravimetric analysis are used to clarify the thermal reducibility of BNF. A relatively good stability of BNF is demonstrated by electrical conductivity and electrochemical impedance spectroscopy measurements. The activity of BNF for oxygen reduction reaction is probed by symmetrical cell and single fuel cell tests. Favorable electrochemical activities at intermediate temperature, *e.g.* very low interfacial resistance of only ~0.016 Ω cm^2 and maximum power density of 1162 mW cm^{-2} at 750 °C, are demonstrated, which could be attributed to the cubic lattice structure of BNF within the temperature range of cell operation.

Introduction

Some composite oxides have defects in their lattice structure,[1] which is the origin of many outstanding properties, such as ionic and electronic conductivity at room or elevated temperature. By making use of those specific properties, many functional applications may be developed. For example, some conducting oxides can be developed into devices for electrochemical energy conversion.[2,3]

With the rapid development in the world's economy, there is a fast expanding demand for energy supply. However, the low efficiency and excessive use of fossil fuels introduce severe problems of environmental pollution, global warming and high risk of an energy crisis. To realize a sustainable future, it is important to reduce emissions and increase efficiency during energy consumption. Electrochemical energy conversion is emerged as a highly promising way for green electric power generation from fossil fuels and renewable energy with much less impact on the environment and significantly improved efficiency.[4,5] In particular, solid oxide fuel cells (SOFCs) have attracted considerable attention recently for their fuel flexibility.[6,7]

In order to make the SOFC technology economically more competitive with currently matured power generation technologies based on fossil fuels combustion, it is important to substantially reduce the cost and increase the operational lifetime. A key factor to meet the above requirements is to decrease the operation temperature to the intermediate range since it can effectively lower the fabrication cost and improve the long-term stability.[8] Similar to other types of fuel cell, a typical SOFC is composed of a porous cathode, a dense electrolyte and a porous anode. The cathode serves as an electrocatalyst for reduction of molecular oxygen to oxygen ions, while the anode is the place for the electro-oxidation of fuel and the electrolyte is an ionic conductor allowing only oxygen ions to transport through. A major challenge for reducing the operation temperature of SOFCs is the quick increase in cathode polarization resistance due to the fact that electrochemical reduction of oxygen is difficult and typically requires high activation energy.[9] During the past, cobalt-containing perovskite oxides, such as $Ba_xSr_{1-x}Co_yFe_{1-y}O_{3-\delta}$,[10,11] $Sm_xSr_{1-x}CoO_{3-\delta}$,[12,13] $La_xSr_{1-x}Co_yFe_{1-y}O_{3-\delta}$,[14,15] and $LnBaCo_2O_{5+\delta}$,[16,17] have been extensively exploited as potential cathodes of intermediate

[a]State Key Laboratory of Materials-Oriented Chemical Engineering, College of Chemistry & Chemical Engineering, Nanjing University of Technology, No. 5 Xin Mofan Road, Nanjing, 210009, PR China. E-mail: ranr@njut.edu.cn; shaozp@njut.edu.cn; Fax: +86 25 83172242; Tel: +86 25 83172256

[b]Department of Chemical Engineering, Curtin University, WA 6845, Australia

temperature (IT)-SOFCs, owing to their high mixed conductivity and prominent electrochemical activity for oxygen reduction reaction (ORR). However, due to the high redox capability and large variation in ionic radius associated with the change in oxidation state and spin state of cobalt ions and high chemical reactivity of cobalt-containing perovskites, such electrodes usually show poor chemical stability and thermal and chemical compatibility with zirconia-based electrolytes, strongly prohibiting their use in practical devices.

The development of cobalt-free cathodes with improved long-term stability and high compatibility with other cell components as well as favorable electrochemical performance at intermediate temperatures is becoming a new research trend.[18–25] The catalytic activity of a perovskite oxide is mainly determined by its B-site ions.[26] Iron ions have higher chemical stability than cobalt ions, favorable electrochemical activity and more suitable ionic size in the B-site of perovskite. In addition, iron also has much lower price and wider availability than cobalt. Thus, iron-based composite oxides, especially perovskite oxides, have been extensively exploited as potential alternative cathode materials of SOFCs for reduced temperature operation.[21–25] It is well known that enhancement of ionic conductivity of the electrode may increase the electrochemical activity by penetrating the reaction zone more deeply into the electrode interior. A doping strategy is often applied to stabilize the disordered lattice structure. Since oxygen vacancy is typically the oxygen ion charge carrier while a disordered oxygen vacancy can maximize the oxygen ion mobility, the substitution of A and B sites of perovskites with cations of lower valence state to introduce more oxygen vacancies has been a general strategy towards the development of high performance electrodes for IT-SOFCs.

As an important parent oxide, many composite oxides with a large diversity of properties can be developed based on $BaFeO_{3-\delta}$ (BF),[27–30] which is a compound with multiple phase structures, such as triclinic, monoclinic, orthorhombic, cubic and hexagonal structures, depending on the preparation method, thermal history and synthesis conditions.[31–35] Doping strategy has been often adopted to stabilize the cubic lattice structure of the BF oxide. The lattice structure of a perovskite oxide is closely related to its tolerance factor, which is defined as $t = (R_A + R_O)/\sqrt{2}(R_B + R_O)$, where R_A, R_B and R_O are the ionic radii of the A-site, B-site and oxygen ions, respectively. The tolerance factor t should be around one for the formation of the cubic lattice structure. The dopant affects the tolerance factor through its different ionic radius from the substituted cation and/or altering the oxidation state and spin state of B-site cations. In addition, the doping may also affect the cation or oxygen vacancy ordering in the perovskite lattice. As a result, a small amount of cation doping may sometimes result in a significant change in the lattice structure. A typical example is $Ba_{0.95}La_{0.05}FeO_{3-\delta}$ (BLF), in which only 5% of the A-site Ba^{2+} cation in BF was substituted by a smaller cation La^{3+}; however, the cubic lattice structure was successfully stabilized at room temperature.[36] As a result, the resulting composite oxide showed very promising electrochemical activity for ORR at intermediate temperature.

Compared to A-site doping, B-site doping is more versatile since there is a wider range of selection for B-site dopants. In addition, since the catalytic activity of perovskite oxides is mainly related to the B-site cations, the electrocatalytic activity of the electrode materials may also be tailored by proper selection of the B-site dopants. Nb^{5+} is a stable cation which is found to stabilize the perovskite structure against reduction.[37] Preparation and basic characterization of the Nb-doped BF perovskites ($BaNb_xFe_{1-x}O_{3-\delta}$) towards application as ferroelectric materials have been reported in recent years.[38–41] However, their elevated temperature properties are rarely reported in literature.

In this study, a B-site small amount of Nb^{5+} doped BF oxide, *i.e.* $BaNb_{0.05}Fe_{0.95}O_{3-\delta}$ (BNF), is synthesized towards application as a cobalt-free cathode material for SOFCs. The phase structure, structural stability, and thermal reducibility of the BNF cathode are characterized. The correlation between the electrochemical performance and the structural properties is exploited.

Experimental

Materials synthesis and cell fabrication

BNF powder was synthesized by a mechano-chemical activation assisted solid-state reaction method using $BaCO_3$, Nb_2O_5 and Fe_2O_3 oxides as the cation sources. Stoichiometric amounts of raw materials were mixed through high-energy ball milling (Fritsch, Pulverisette 6) at a rotational speed of 400 rpm for 1 h with ethanol as a liquid medium. After drying, the powder mixture was calcined at 1000 °C in air for 10 h. Then, an intermediate grinding by ball milling for 0.5 h was conducted. The primary powder was further calcined at 1200 °C for 10 h under air atmosphere to obtain a final powder for later use.

The BNF colloidal suspension for spray deposition was dispersed in a premixed solution of isopropyl alcohol, ethylene glycol and glycerol, followed by high-energy ball milling at 400 rpm for 0.5 h. Symmetrical cells of BNF|$Sm_{0.2}Ce_{0.8}O_{1.9}$ (SDC)|BNF configuration were fabricated through painting BNF slurry onto both surfaces of dense SDC pellets and then firing the sprayed cells at 1000 °C for 2 h.

The Ni–$Y_{0.16}Zr_{0.92}O_{2.08}$ (YSZ) anode substrates were prepared by a tape casting process. Circular anode substrates with 16 mm diameter were drilled from the tape by a punch, followed by pre-firing at 1100 °C in air to remove organic residues. The YSZ|SDC double electrolyte layers were prepared *via* wet powder spraying. The YSZ and SDC powders were suspended in ethylene glycol in an 80 mL zirconia container and agitated on a high-energy ball mill with a rotational speed of 400 rpm for 0.5 h. The weight percentages of YSZ and SDC powders in the colloidal suspensions were both about 5%. To fabricate the dual-layer thin-film electrolytes, the YSZ suspension was firstly sprayed with 1 atm nitrogen as carrier gas onto the anode substrate using a spraying gun (HD-130 A). The spraying gun was aligned vertically to the heated anode substrate (~200 °C on a hot plate) leaving a distance of ~10 mm. After the spray deposition, the dual-layer pellets were then fired at 1400 °C for 5 h at a heating rate of 5 °C min^{-1}, with the subsequent repeated procedure for SDC

buffering layer and following calcination at 1350 °C for 5 h. The BNF slurry was then painted onto the central surface of the SDC electrolyte and calcined at 1000 °C for 2 h under an air atmosphere to function as the cathode layer.

Characterization

The phase structure of BNF oxide was determined by X-ray diffraction (XRD, Rigaku Smartlab) with filtered Cu-Kα radiation. An *in situ* high-temperature X-ray diffractometer (HT-XRD, Philips, X'Pert Pr) was utilized to measure the structural evolution of powders across a temperature cycle from room temperature to 900 °C in air with a heating and cooling rate of 5 °C min^{-1}. Le Bail/Rietveld refinements on the XRD patterns were conducted using General Structure Analysis System (GSAS) software. Transmission electron microscopy (TEM) was employed to determine the crystal structure of BNF with an FEI Tecnai G2T20 electron microscope operating at 200 kV.

The oxygen temperature-programmed desorption (O_2-TPD) was carried out to investigate the reduction behaviour of transition metal *e.g.* iron ions in perovskite using a mass spectrometer (MS Hiden QIC-20). Approximately 150 mg of the powder was loaded in a quartz tube. The assembly was placed in a tubular furnace equipped with a temperature controller. Pure argon at a flow rate of 15 mL min^{-1} [STP] served as the carrier gas. The temperature was programmatically raised from room temperature to 930 °C at a ramp rate of 10 °C min^{-1}. The high-temperature oxygen non-stoichiometry and average oxidation state of iron ions in BNF powder were characterized by thermo-gravimetric analysis (TGA, Netzsch, STA 449 F3) after consideration of oxygen non-stoichiometry at room temperature obtained by iodometric titration. TGA was carried out under air flow rate of 50 mL min^{-1} between room temperature and 1000 °C. For a typical iodometric titration, approximately 0.1 g of the BNF powder was dissolved in dilute hydrochloric acid before titration with a standardized thiosulfate solution. Several drops of starch solution were added as titration indicator when the reactive solution changed its color abruptly. A coin-shaped BNF powder with 1 mm thickness as a yardstick was sintered for the thermal expansion coefficient (TEC) measure, which was conducted using a Netzsch DIL 402C/3/G dilatometer in flowing air from room temperature to 1000 °C.

The bar-shaped BNF with 2 mm × 5 mm × 12 mm dimensions was prepared by dry pressing followed by sintering at 1250 °C for 5 h for conductivity testing. The electrical conductivity was determined based on a four-probe DC configuration using a Keithley 2420 source meter within the temperature range of 300–900 °C at intervals of 10 °C. The chemical bulk diffusion coefficient (D_{chem}) and the chemical surface exchange coefficient (k_{chem}) of BNF were obtained using the electrical conductivity relaxation (ECR) technique. A sudden change in the oxygen partial pressure, *e.g.* from 0.1 to 0.21 atm, was created by switching from one gas to another abruptly. The time dependence of conductivity was performed through the aforementioned technique and the measurement was conducted between 750 and 550 °C at intervals of 50 °C. After each temperature change, the sample was stabilized for at least 1 h before later measurement.

Electrochemical measurements

The electrochemical impedance spectra (EIS) of the symmetric cells were obtained using an electrochemical workstation based on a Solartron 1287 potentiostat and a 1260 A frequency response analyzer. The frequency range was applied from 100 kHz to 0.1 Hz with the signal amplitude of 10 mV under open circuit voltage (OCV) conditions. *I–V* polarization was measured for assessing the performance of the coin-shaped single fuel cell within the temperature range of 550–750 °C using a Keithley 2420 source meter. The anode side and cathode side were supplied with H_2 fuel at a flow rate of 80 mL min^{-1} [STP] and ambient air, respectively.

Results and discussion

The cathode in a SOFC acts as the electrocatalyst for the reduction of molecular oxygen to oxygen ions. The ORR involves several intermediate steps, including oxygen gas phase diffusion, surface adsorption, surface diffusion, dissociation and charge transfer. Each step may be the rate limiting step to introduce electrode polarization. Except for the gas phase diffusion, all the other steps are strongly dependent on composition and lattice structure of the electrode materials. In addition, the operational stability is also closely related to the phase stability of the electrode materials. For example, a first-order phase transition may introduce large variation in lattice volume to induce big internal stress of the electrode, which can cause the delamination of the electrode layer from the electrolyte surface or the damage of the electrode microstructure by pulverization during the long-term operation, thus the performance decay. Under real fuel cell operation conditions, the electrode may experience a large variation in oxygen partial pressure and temperature, while the phase structure of the BF parent oxide is very sensitive to environmental conditions, thus the doping strategy was often tried to stabilize its most favorable phase structure. For the B-site doping, Zr, Ce, Yi, Cu and Ni were found to be favorable dopants.[42–45]

To demonstrate the effectiveness for stabilizing the cubic phase structure of BF by doping the B-site with small amounts of Nb^{5+}, initially the room-temperature XRD patterns of BNF and BF parent oxide were comparatively studied. Since the phase structure may be sensitive to synthesis conditions, some particular treatments were given to detect the phase structural alteration of the BF specimen. Here the BF sample was calcined at 1000 °C in air for 5 h and cooled to room temperature in air naturally, and aging at room temperature in air for one week was performed to ensure the equilibrium of the oxygen content in the sample with the ambient environment. As shown in Fig. 1a, for the BF parent oxide, the diffraction peaks are very different from that of a standard oxygen vacancy-disordered cubic perovskite structure. A combined Rietveld/Le Bail whole pattern decomposition method was then applied to refine the unit cell and the Le Bail method was applied to fit a monoclinic phase with space group of $P121/c1$. A cubic phase (space group $Pm\bar{3}m$, $a = b = c = 3.996(6)$ Å), a rhombohedral phase (space group $Cmc2_1$, $a = 8.449(0)$ Å, $b = 19.043(6)$ Å, $c = 5.377(6)$ Å) and

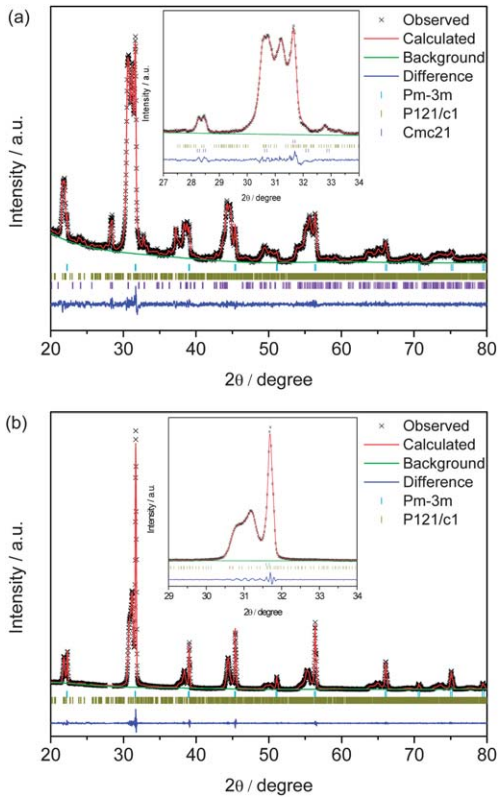

Fig. 1 Combined Rietveld/Le Bail refinements of XRD patterns of (a) BF and (b) BNF powders at room temperature with magnified XRD patterns of specific angle ranges.

a monoclinic phase (space group $P121/c1$, $a = 7.018(7)$ Å, $b = 11.724(9)$ Å, $c = 23.326(5)$ Å) with low reliability factors of $R_{wp} = 4.08\%$, $R_p = 3.06\%$ and $\chi^2 = 1.323$ obtained from the refinement in Fig. 1a was found to best fit the observed patterns. From our previous study, these three phases could be $BaFeO_3$, $BaFe_2O_4$ and $Ba_2Fe_2O_5$,[46] respectively. The composition of BF in this study was slightly different from a similar sample prepared from the high-temperature calcination without the step of long-term aging at room temperature in our previous study.[36] It further supported the sensitivity of the phase structure of BF to the synthesis conditions and thermal history. As shown in Fig. 1b, after doping the iron site with only 5% Nb^{5+}, the XRD patterns changed significantly, becoming more similar to the cubic phase. According to the combined Rietveld/Le Bail refinement, the composite was composed of a cubic phase (space group $Pm\bar{3}m$, $a = b = c = 4.002(1)$ Å) and a monoclinic phase (space group $P121/c1$, $a = 6.990(0)$ Å, $b = 11.744(6)$ Å, $c = 23.327(2)$ Å) possibly expressed as $BaNb_xFe_{1-x}O_{3-\delta}$ and $Ba_2Nb_yFe_{2-y}O_{5-\delta}$, respectively. The low converged reliability factors (*e.g.* $R_{wp} = 4.25\%$, $R_p = 3.13\%$ and $\chi^2 = 1.324$) indicate a good fitting between the experimental and calculated patterns. It should be noted that the contribution of the monoclinic phase to the power profile is also fitted with the Le Bail method. Although the minor amount (5%) of Nb^{5+} doping still failed to totally stabilize the cubic phase down to room temperature, the BNF powder has a relatively preferable diffractive profile and peak intensity of perovskite structure compared to the BF sample. Thus Nb^{5+} might still be a favorable dopant for BF.

To perform as a cathode material, a cubic phase is preferable under the operation conditions since it can maximize the mobility of oxygen ions and electrons. To get information about the phase evolution of BNF with respect to temperature, HT-XRD patterns of BNF powder in air were then characterized. Fig. 2a and b depict the *in situ* XRD patterns of BNF powder on heating from room temperature to 900 °C at a rate of 5 °C min^{-1}, and the reverse process by decreasing the temperature to room temperature, respectively. The intensity of the monoclinic phase decreased steadily with increasing temperature and became near zero at ~400 °C. Thereafter, the cubic structure was maintained at temperatures up to 900 °C, the highest temperature that was investigated in this study. Taking BNF at 700 °C as an example, as shown in Fig. 3, Rietveld refinement confirmed that all the diffraction peaks were well indexed based on an oxygen vacancy-disordered cubic perovskite (space group $Pm\bar{3}m$) with the affordable reliability factors of $R_{wp} = 9.15\%$, $R_p = 8.84\%$ and $\chi^2 = 1.016$. Thus, under SOFC operation conditions, the BNF actually took the cubic perovskite structure although a mixture phase was observed at room temperature. It is interesting that the phase transition between monoclinic and cubic phases within the temperature range from 400 °C to room temperature as appeared in the first heating process was not observed during the cooling process. As shown in Fig. 2b, BNF maintained its cubic perovskite lattice structure even at room

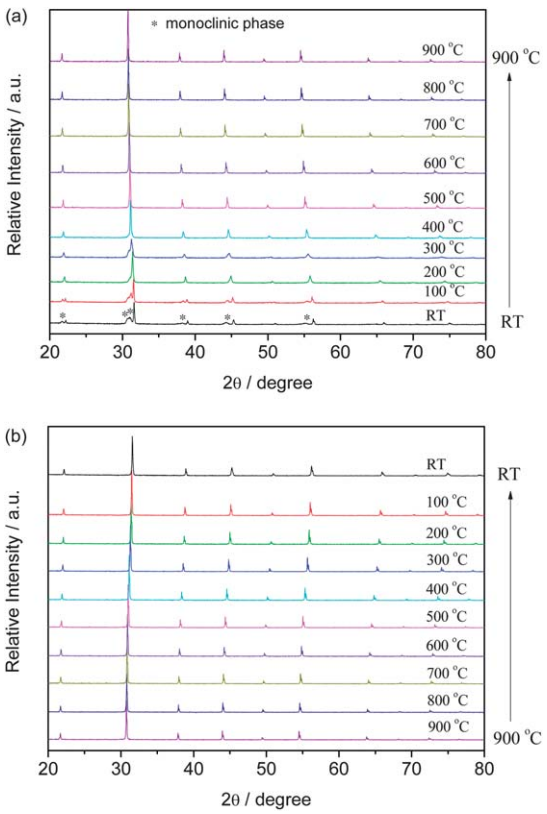

Fig. 2 HT-XRD patterns of BNF powder: (a) heating from room temperature to 900 °C at 5 °C min^{-1}, (b) cooling from 900 °C to room temperature at 5 °C min^{-1}.

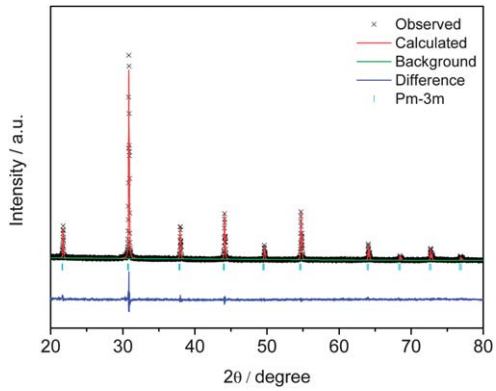

Fig. 3 Rietveld refinement of *in situ* XRD pattern of BNF powders at 700 °C.

temperature upon cooling from 900 °C. It implies the transition of the cubic phase to the monoclinic structure was kinetically slow at reduced temperature, which was probably caused by the slower equilibration of the oxygen in BNF with the ambient environment during cooling due to the fast cooling rate.

To get more information about the local crystal structure, BNF particles were also characterized by TEM. The high resolution TEM (HR-TEM), selected area electron diffraction (SAED) and the corresponding Fourier transform (FT) of room-temperature BNF powder and the sample quenched from 700 °C in air are shown in Fig. 4 and 5, respectively. It is explicit that the accurate SAED pattern can be acquired when it is aligned to a specific zone axis (perpendicular to the direction of the plane for diffraction pattern). The SAED and HR-TEM are complementary to each other only while the TEM image is corresponding to the SAED pattern with the specific zone axis direction [*r s t*], which can be determined by the calibration of the indices of crystal plane (*h k l*) for two non-collinear diffraction spots according to the law of zone. For the room-temperature sample, there was a plurality of different streaks in the crystal lattice, detected by two micro-zones from the same film (Fig. 4b and c). A somewhat regular dot array could be seen from the SAED; however, various small clutter-spots arranged approximately in a ring existed in the vicinity of the bright central spot. With regard to the corresponding FT, the image was indeed not indexed based on a single phase in contrast to the standard spectrum. By means of measuring the distances between the diffraction spots and the bright central spot, it is found that the small clutter-spots represent the different crystal planes derived from different crystal phases. Combining with the crystalline fringes with different *d* lattice spacing values (not belonging to the same phase), accordingly, we can take it as read that the BNF is composed of non-single phase at room temperature, in good agreement with the XRD results. For the sample quenched at 700 °C, the similar lattice spacing (~0.338 nm) from different axial orientations was observed through selecting two different regions as shown in Fig. 5a and b, which, together with SAED and FT (Fig. 5e and f), is a strong indicator that the sample was likely composed of a single phase with cubic structure, in accordance with the XRD results. However, from the SAED pattern, it seems there are some extra

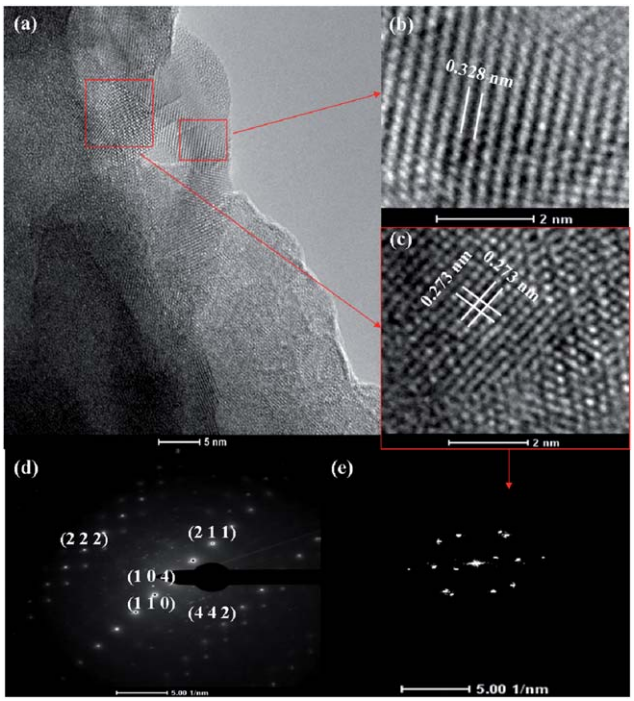

Fig. 4 (a) Typical HR-TEM images of BNF at room temperature; (b and c) the magnified HR-TEM images showing lattice fringes; (d and e) the SAED and corresponding FT patterns.

spots showing there, which could be attributed to various possible reasons including the existence of other grains due to the defective structure probably generated during the quenching process and the high-order Laue zone induced by the slightly thick specimen. Furthermore, the transition from the mixture phase at room temperature to the single cubic phase at elevated temperature can also be reflected by the larger lattice spacing (HR-TEM) and preferable lattice symmetry (SAED and FT) of the quenched sample at 700 °C compared with that at room temperature.

To exploit the origin of the thermally induced phase transition for the BNF sample, a combination of O_2-TPD, TGA and thermal expansion measurements were conducted. As shown in Fig. 6, with the programmatic increase of temperature, obvious oxygen desorption started at 380 °C which peaked at 480 °C in the O_2-TPD profile was observed; even at 930 °C, the highest temperature examined, the oxygen release still happened. In the TGA profile (Fig. 7), obvious weight loss was initialized at around 440 °C and the weight loss continued up to 1000 °C, the highest examined temperature in this study, to reach a total weight loss of 1.4% in the TGA curve. A slight increase in slope of the dilatometric curve was observed between 380 and 450 °C (Fig. 8). In combination with the O_2-TPD, it is clear that the weight loss in TGA is due to the oxygen release from the oxide lattice. It should be mentioned that the oxygen release could be kinetically controlled; the exact starting temperature for oxygen release as demonstrated in TGA and O_2-TPD could be slightly different due to their different experimental conditions. As we know, the depletion of oxygen from oxide lattice should be

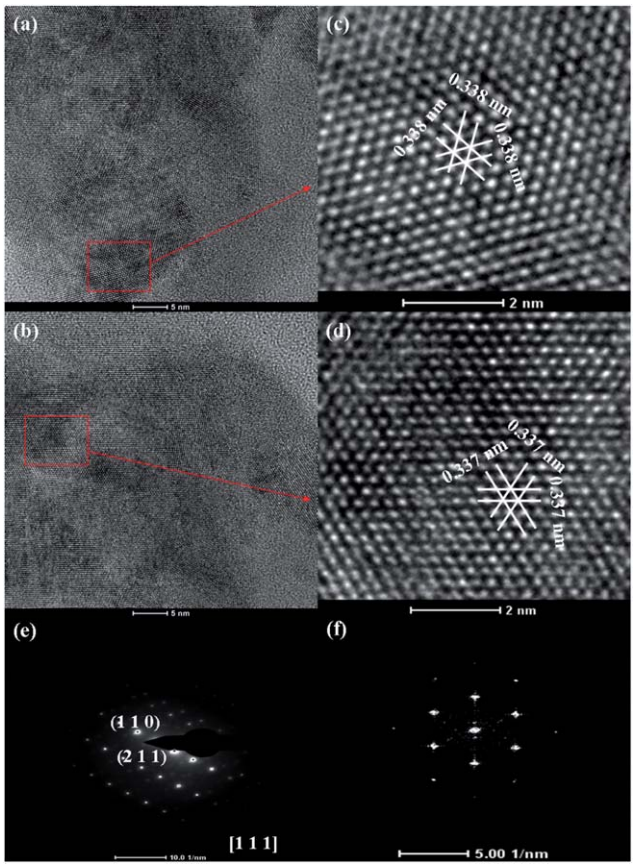

Fig. 5 (a) Typical HR-TEM images of BNF quenched at 700 °C; (b and c) the magnified HR-TEM images showing lattice fringes; (d and e) the SAED and corresponding FT patterns.

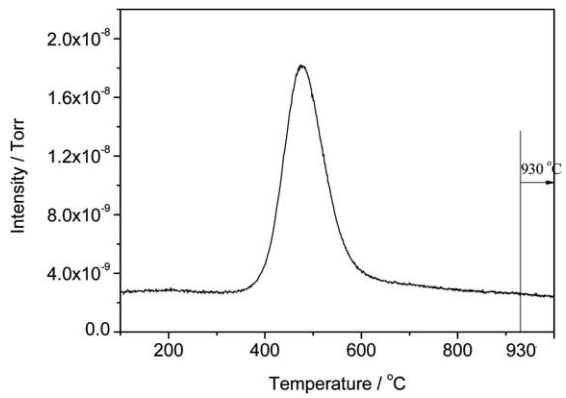

Fig. 6 O_2-TPD profile of BNF.

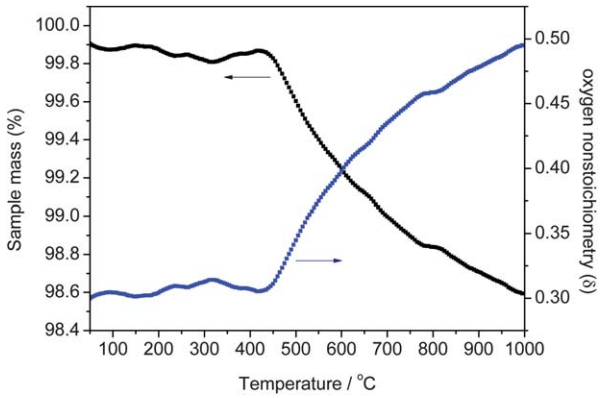

Fig. 7 Thermal analysis and oxygen non-stoichiometry of BNF as a function of temperature.

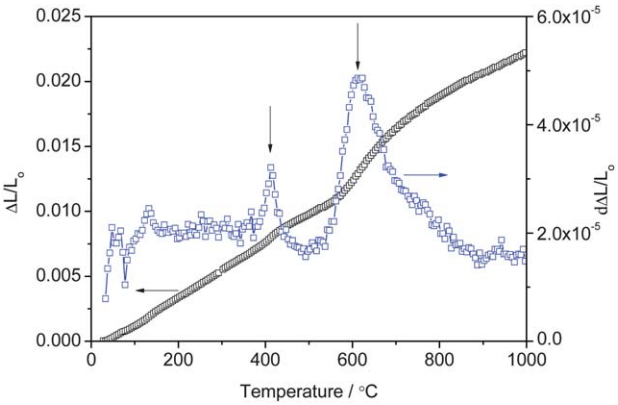

Fig. 8 Thermal expansion behavior of BNF.

accompanied by the thermal reduction of variable cations to maintain the local electrical neutrality. Thus, iron ions in the B-site of the perovskite started to be partially reduced to lower oxidation states at temperatures higher than 380 °C, resulting in increased ionic size to induce a chemical expansion of the oxide lattice; this is the origin of the small inflection of the dilatometric curve at around 400 °C (Fig. 8). The oxygen release also means the creation of additional oxygen vacancies in the oxide lattice. The dependence of oxygen vacancy concentration (δ) on temperature was obtained by TGA in air (Fig. 7). The δ value at room temperature, determined by iodometric titration, was 0.286 for the room-temperature sample, while it increased steadily with temperature and reached 0.459 at 800 °C. In general, a higher oxygen vacancy concentration benefits the oxygen ion transport since oxygen vacancy is the oxygen-ion charge carrier. Based on the oxygen non-stoichiometry, the average valence state of iron ions was found to reduce from 3.35 at room temperature to 2.98 at 800 °C, suggesting the increased content of trivalent iron and the reduced tetravalent iron at higher temperature. It is known that the Fe^{4+} (d^4) and Fe^{3+} (d^5) electronic configurations are best accommodated by the square-pyramidal [FeO_5] and octahedral [FeO_6] sites, respectively, in view of the crystal-field stabilization energy.[47] Thus the reduction of Fe^{4+} to Fe^{3+} should favor the formation of the corner-shared [BO_6] structure. In addition, the increase in ionic radius of iron and the elongation of the (Fe,Nb)–O bond due to the thermal reduction of iron ions should diminish the discrepancy between the length of the (Fe,Nb)–O bond and the Ba–O bond. Both factors facilitated the formation of a cubic perovskite structure. The weight loss started at around 400 °C, in good agreement with the full formation of the cubic lattice structure. It further supports our hypothesis that the phase transition of

BNF from monoclinic to cubic structure is promoted by the reduction of Fe^{4+} to Fe^{3+}. As shown in Fig. 8, in addition to the inflection in the dilatometric curve at ~400 °C, an additional more obvious inflection point at around 600 °C appeared. The Fe^{3+} ions experience a low spin ($Fe_{LS}^{3+}((t_{2g}^{+})^3(t_{2g}^{-})^2)$) to high spin ($Fe_{HS}^{3+}((t_{2g}^{+})^3(e_g^{+})^2)$) transition as the temperature increases due to the thermal excitation. At low temperatures, Fe^{3+} ions are in low spin states. Due to the small energy difference between the low-energy and high-energy states, Fe^{3+} ions can be thermally excited to high spin states at elevated temperatures. Considering the larger ionic radius of the Fe_{HS}^{3+} (0.645 Å) compared to that of the Fe_{LS}^{3+} (0.55 Å), the TEC inflection at around 600 °C is likely contributed from the spin state transition. In simple terms, the appearance/increase of thermal population of high spin states for Fe^{3+} contributes to the thermal expansion because these states have a larger ionic radius with respect to Fe_{LS}^{3+}. As a result, the increased thermal population of Fe_{HS}^{3+}, with a larger ionic radius, would lead to the magnetic contribution to thermal expansion (usually being composed of three components: phonons, magnetism and oxygen vacancies), which can also be interpreted by the magnetic contribution to the thermal expansion:[48]

$$\alpha_{mag} = x_{HS}\frac{1}{3}(r_{HS} - r_{LS})\ \frac{1}{V}\frac{\partial V}{\partial r} \quad (1)$$

where α_{mag} is the TEC, x_{HS} is the fraction of high-spin species, r_{HS} and r_{LS} are the ionic radii of Fe_{HS}^{3+} and Fe_{LS}^{3+} species, respectively.

As mentioned, the transport properties of composite oxides are closely related to their phase structures. $BaFeO_3$-based oxides are typically mixed conductors with overwhelming electronic conductivity. Thus the electrical conductivity measured by the four-probe DC method mainly embodies the electronic conductivity. The electrons in perovskite or related structured oxides are conducted mainly through small polaron hopping *via* the strong overlapping of the outer orbitals of B-site cations and oxygen ions along B–O–B chains, which comprises the principally collinear overlap between the p_σ orbitals of B-site cations and p_σ orbitals of oxygen ion and non-collinear overlap between the t_{2g} orbitals of B-site cations and p_π orbitals of oxygen ions. The d-electrons in p_σ/t_{2g} orbital of B-site cation are permitted to drift into the p_σ/t_{2g} orbital of a neighboring B-site cation through the p_σ/p_π orbital of the intermediate oxygen ion. Therefore, these itinerant electrons would give rise to electron/hole transport. The change in the lattice structure leads to a change of B–O bond length and B–O–B bond angle. Along with this change, the electron cloud density and d-orbital overlap between B-site cations and oxygen ions are changed, and hence the charge transfer interaction is affected. Eventually, a change in the conductivity may be induced. Thus, the change in behavior of electrical conductivity with respect to temperature may also be an indication of the phase transition. The electrical conductivity of BNF was measured by the following manner to analyze the potential phase transition. It was first measured from 300 to 900 °C at intervals of 10 °C during the progressive increase of temperature at a rate of 5 °C min^{-1}, and 5 min was allowed for stabilization at each measured temperature. After reaching 900 °C, the conductivity was further measured during the cooling process at intervals of 10 °C till 300 °C. The conductivity was measured in ambient air during the heating–cooling cycles with the results presented in Fig. 9. Based on the conductivity data, several rules can be derived. As a whole, a first increase in electrical conductivity with temperature until a maximum conductivity then a decrease in conductivity with the further increase in temperature was observed, no matter whether the conductivity was measured during the heating or cooling processes and the exact measurement cycle. However, slightly different shapes of the conductivity curves were observed for the heating and cooling processes, and also between the conductivity curves measured from the first heating process and the following heating processes. At temperatures lower than 550 °C, the conductivity measured in the first heating process was much lower than that measured in the second heating process; in addition, the maximum conductivity measured during the first heating process was reached at 640 °C, which is much higher than 550 °C for that measured during the following heating processes. The conductivity curves were perfectly overlapped for those measured during the second, third and fourth heating processes, and also for those measured during the cooling processes. The conductivity is closely related to phase structure of the oxides, and phase transition and variation in oxidation state of the compositional elements could induce a change in conductivity. Since all the other conductivity curves measured during heating were overlapped except that from the first heating process, it strongly suggested a phase transition appeared during the first heating process, while no more phase transition appeared during the subsequent heating–cooling cycles, in good accordance with the XRD results. It was interesting that the conductivity curves measured from heating and cooling processes were overlapped at the low temperature zone (300–500 °C) and high temperature zone (700–900 °C), while larger conductivity for that measured from the heating than that from cooling was observed at the intermediate temperature zone (500–700 °C). It is well known that the conductivity is also closely related to oxygen content inside the oxide lattice. The thermal reduction of iron ions would create more oxygen vacancies, which is accompanied by a

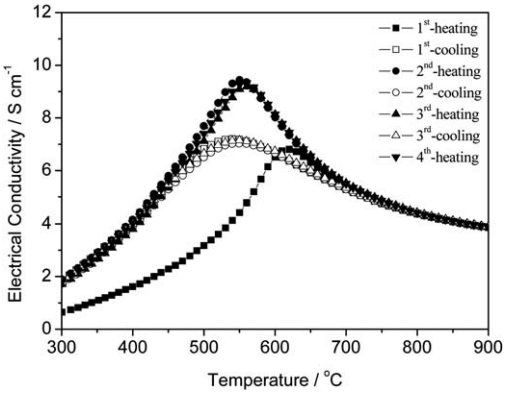

Fig. 9 The temperature dependence of electrical conductivities of BNF measured in ambient air during the heating–cooling cycles.

reduced number of electrons/holes acting as the charge carriers (for each oxygen ion leaving the lattice two electron holes are eliminated), thus having a detrimental effect on the electronic conductivity. On the other hand, small polaron hopping is thermally activated, so an increase in conductivity with temperature is expected. The actual dependence on the temperature is a balance of both factors. It suggests that a small hysteresis effect upon heating and cooling was likely for BNF due to the failure to reach complete equilibrium of the oxygen stoichiometry during heating and cooling. Within the intermediate temperature range, the oxygen content in BNF was likely higher from heating than that from cooling due to the hysteresis effect, thus higher conductivity was observed during the heating process. Anyway, BNF demonstrated only modest electrical conductivity of 4–10 S cm^{-1} within the intermediate temperature range (500–800 °C), similar to the A-site La^{3+} doped BF (BLF), which was reported to have electrical conductivity of 4–11 S cm^{-1} within the temperature range of 300–900 °C.[36]

Based on the above analysis, it is clear that an oxygen vacancy disordered cubic perovskite was formed within the intermediate temperature range of 500–800 °C, although the BNF oxide was composed of a mixture phase at room temperature. It is well known that the performance of a mixed conducting electrode for ORR is closely related to its surface exchange kinetics and bulk diffusion properties. The cubic phase favors oxygen surface exchange and oxygen bulk diffusion. The surface and bulk properties of BNF within intermediate temperature range were then measured by the ECR method. Fig. 10 demonstrates the ECR response curves at various temperatures after a sudden change of the oxygen partial pressure from 0.1 to 0.21 atm and the temperature dependence of the fitted D_{chem} and k_{chem} of BNF oxide. Judging by the temperature dependence of D_{chem} and k_{chem} (excluding $T = 550$ °C), both D_{chem} and k_{chem} values rise with an increase in temperature, and the activation energies are $\sim 186 \pm 6$ and $\sim 184 \pm 8$ kJ mol^{-1}, respectively. The activation energy value for k_{chem} is quite similar to that reported for $La_{0.6}Sr_{0.4}Co_{0.8}Fe_{0.2}O_{3-\delta}$ (LSCF ~190 kJ mol^{-1}) obtained with the weight relaxation method.[49] It is remarkable that the surface exchange process has virtually the same activation energy value as LSCF. At 750 °C, D_{chem} and k_{chem} values of 2.47×10^{-4} cm^2 s^{-1} and 2.62×10^{-3} cm s^{-1}, respectively, are obtained, which are comparable to several well-studied perovskite cathodes, such as $Bi_{0.5}Sr_{0.5}FeO_{3-\delta}$ (BSF) and $Ba_{0.5}Sr_{0.5}Co_{0.8}Fe_{0.2}O_{3-\delta}$ (BSCF).[50,51] It suggests BNF may perform well for ORR at intermediate temperatures.

The performance of BNF as electrocatalyst for ORR was first tested in symmetric cell configuration with thick SDC electrolyte. The measurement was conducted in air atmosphere and under open circuit conditions. Fig. 11 shows the typical EIS measured at 700 °C and the inserted temperature dependence of area specific resistances (ASRs) of the BNF|SDC|BNF symmetric cell between 550 and 750 °C. The measurements were conducted from high to low temperature, since a hysteresis effect in oxygen content may exist in BNF. At each point, several tests were performed until a stable value was reached. The ASRs are 0.427, 0.147, 0.058, 0.026 and 0.016 Ω cm^2 at 550, 600, 650, 700 and 750 °C, respectively. A good single linearity of

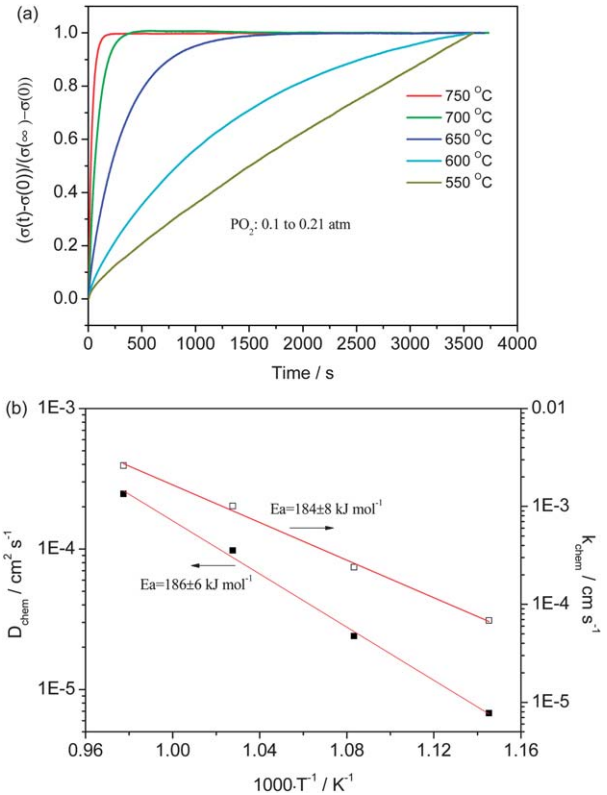

Fig. 10 ECR response curves of BNF at various temperatures after a sudden change of oxygen partial pressure from 0.1 to 0.21 atm (a), and the temperature dependence of the fitted D_{chem} and k_{chem} (b).

the cathode ASR *versus* reciprocal temperature implies that the same reaction mechanism controls the overall electrode behavior over the temperature range investigated. The derived activation energy, ~117 kJ mol^{-1}, was significantly lower than that determined for the oxygen diffusion step (D_{chem}) and oxygen surface exchange step (k_{chem}). Such low activation energy, meaning the low temperature dependence of the ASR, is desirable to overcome the effect of reducing the operation

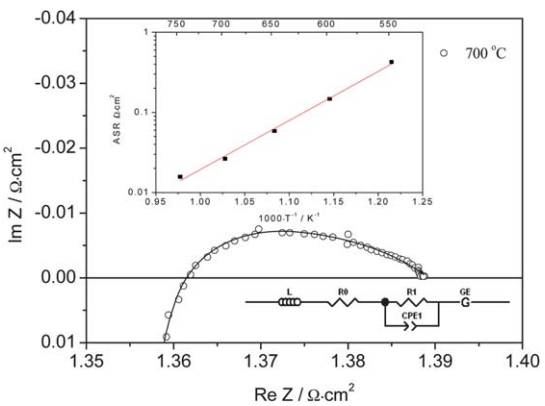

Fig. 11 The Nyquist impedance curve for the symmetric cell BLF|SDC|BLF measured at 700 °C. The inset is testing temperature dependence of the impedance for BLF between 550 and 750 °C and the equivalent circuit adopted for fitting the EIS data.

temperature on the final cathode performance, which is of interest for reduced temperature operation. A comparison of the ASRs for different iron-based electrodes is listed in Table 1. It demonstrates the BNF electrode is among the most active electrocatalysts for ORR. It is likely due to the high oxygen vacancy concentration inside the oxide lattice as well as cubic phase structure under the operation conditions. It was found that the experimental data (hollow circles) can be fitted well by the simulated curve (solid line) obtained from the electrical equivalent circuit model with a configuration of L–R_o–(R_1–CPE_1)–G (inset in Fig. 11). The high frequency arc is a depressed semicircle which can be modeled as a parallel combination of a resistor (R_1) with a constant phase element (CPE_1). The low frequency arc can be predicted as a Gerischer element (G), whose mathematical formula is described by:

$$Z_G = \frac{Z_o}{\sqrt{k + jw}} \quad (2)$$

where Z_o is a resistance-like resistance and k is a reaction rate constant. This reaction rate constant (k) is an indicator of the limiting process of the ORR on mixed ionic–electronic conductors where a competition between bulk and surface diffusion take place at the same time. Adler *et al.*[52,53] have derived a model, referred to as the ALS model, that couples the oxygen surface exchange with oxide ion diffusion into one electrochemical response. This response takes the form of a Gerischer impedance. The coupling within a mixed conducting electrode can be rationalized as the reaction is believed to proceed over a larger fraction of the surface rather than just at the three-phase boundary (TPB). As the impedance data are accurately modeled with the Gerischer element, a chemical–electrochemical–chemical type reaction is expected at the mixed ionic–electronic conducting cathode.

As demonstrated previously, BNF may show a phase transition at temperatures lower than 400 °C. However, the phase transition was not observed during the cooling process and BNF could keep its cubic perovskite structure in the subsequent period after high-temperature operation. Thus a good performance stability is still expected. The performance stability of the BNF electrode for oxygen reduction was then investigated by the symmetric cell test under repeated thermal cycles. The symmetric cell was heated from room temperature to 700 °C at a rate of 10 °C min^{-1}, held at 700 °C for half an hour to allow the oxygen content to reach its equilibrium; after the EIS measurement, the temperature was decreased to 300 °C at the same rate and then heated to 700 °C again. The thermal cycles were repeated fifteen times. Fig. 12 shows the ASR of the BNF electrode as a function of cycling numbers at 700 °C under OCV conditions. The electrode ASR maintained at around 0.02 Ω cm^2 during the thermal cycles, in spite of a minor downward trend at the early cycle stage. It suggests BNF can be stably operated irrespective of potential phase transition.

The performance of BNF for ORR was further investigated in a single fuel cell under real fuel cell operation conditions. Here an anode-supported cell with the configuration of Ni–YSZ|YSZ (~15 μm)|SDC (~5 μm)|BNF was fabricated. Air served as the cathode atmosphere while hydrogen was the fuel. Fig. 13 shows the *I–V* and *I–P* curves of the cell at different temperatures. The maximum power densities were 1162, 881, 564, 335 and 180 mW cm^{-2} at750, 700, 650, 600 and 550 °C, respectively, which are comparable to similar cells with other high-performance cathodes like BSF and BLF.[25,36] The power output is also only slightly lower than similar cells with cobalt-based electrodes like BSCF, $SrSc_{0.2}Co_{0.8}O_{3-\delta}$ and $Sm_{0.5}Sr_{0.5}CoO_{3-\delta}$.[10,59,60] It further promises BNF as a potential high-performance cobalt-free electrode of IT-SOFCs. The positive contribution from the

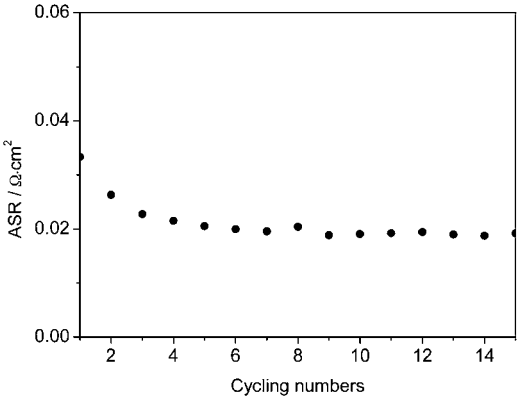

Fig. 12 ASR of BNF electrode as a function of cycling numbers operated at 700 °C under OCV conditions during thermal cycles between 300 °C and 700 °C.

Table 1 ASRs for different iron-based electrodes based on symmetric cells

Cathode	Electrolyte	Operating temperature (°C)	ASR (Ω cm^2)	Ref.
$Sr_2Fe_{1.5}Mo_{0.5}O_{6-\delta}$	LSGM[a]	700	1.94[b]	23
$Ba_{0.5}Sr_{0.5}Zn_{0.2}Fe_{0.8}O_{3-\delta}$	SDC	700	0.23	24
$Bi_{0.5}Sr_{0.5}FeO_{3-\delta}$	SDC	700	0.12	25
$La_{0.5}Sr_{0.5}FeO_{3-\delta}$	SDC	700	0.79	50
$Pr_{0.8}Sr_{0.2}FeO_3$	YSZ	700	1.96[b]	54
$SrNb_{0.1}Fe_{0.9}O_{3-\delta}$	SDC	700	0.058	55
$La_{0.6}Sr_{0.4}Fe_{0.8}Cu_{0.2}O_{3-\delta}$	SDC	700	0.306	56
$Ba_{0.5}Sr_{0.5}Fe_{0.9}Nb_{0.1}O_{3-\delta}$	SDC	700	0.035[b]	57
$SmBaFe_2O_{5+\delta}$	SDC	700	0.196	58

[a] $La_{0.8}Sr_{0.2}Ga_{0.87}Mg_{0.13}O_3$. [b] An extrapolation of ASR values to the reference temperature of 700 °C.

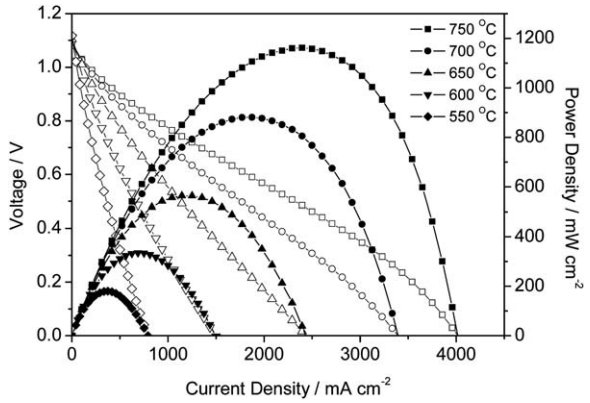

Fig. 13 The *I–V* and *I–P* curves for the complete cell based on Ni–YSZ|YSZ|SDC|BNF.

oxygen vacancy-disordered perovskite oxide with a stable cubic lattice structure within the temperature range of cell operation could account for the superior electrochemical performance.

Conclusion

In summary, we demonstrate a novel minor Nb-substitution for Fe in the B-site of $BaNb_{0.05}Fe_{0.95}O_{3-\delta}$ (BNF) perovskite synthesized by solid state reaction process. The crystal structure, thermal reducibility, structural stability and electrochemical behaviour of BNF have been evaluated. BNF exhibits a phase transformation from multiphase structure comprising a monoclinic phase and a cubic phase at room temperature to cubic structure at approximately 400 °C, the onset temperature of the release of lattice oxygen from the crystal. Thereafter, the cubic structure is maintained upon further heating till 900 °C and subsequent cooling to room temperature, probably caused by the sluggish structural change kinetics at reduced temperature. A relatively stable operation of BNF was confirmed experimentally despite the potential phase transition. Moreover, BNF cathode demonstrates reasonably superior electrochemical performance with interfacial resistance of 0.016 Ω cm^2 and peak power density of 1162 mW cm^{-2} at 750 °C, highlighting the promising application of BNF as a new cathode candidate for IT-SOFCs.

Acknowledgements

This work was supported by the "National Science Foundation for Distinguished Young Scholars of China" under contract no. 51025209 and by the "Australian Research Council future fellowship".

Notes and references

1 J. Mizusaki, N. Mori, H. Takai, Y. Yonemura, H. Minamiue, H. Tagaw, M. Dokiy, H. Inaba, K. Naraya, T. Sasamoto and T. Hashimoto, *Solid State Ionics*, 2000, **129**, 163.
2 B. C. H. Steele and A. Heinzel, *Nature*, 2001, **414**, 345.
3 B. Zhao, X. Yu, R. Cai, R. Ran, H. Wang and Z. Shao, *J. Mater. Chem.*, 2012, **22**, 2900.
4 B. C. H. Steele, *Nature*, 1999, **400**, 619.
5 P. V. Kamat, *J. Phys. Chem. C*, 2007, **111**, 2834.
6 Z. Shao, S. M. Haile, J. Ahn, P. D. Ronney, Z. Zhan and S. A. Barnett, *Nature*, 2005, **435**, 795.
7 Z. Zhan and S. A. Barnett, *Science*, 2005, **308**, 844.
8 D. J. L. Brett, A. Atkinson, N. P. Brandon and S. J. Skinner, *Chem. Soc. Rev.*, 2008, **37**, 1568.
9 S. B. Adler, *Chem. Rev.*, 2004, **104**, 4791.
10 Z. Shao and S. M. Haile, *Nature*, 2004, **431**, 170.
11 W. Zhou, R. Ran, Z. Shao, R. Cai, W. Jin, N. Xu and J. Ahn, *Electrochim. Acta*, 2008, **53**, 4370.
12 C. Xia, W. Rauch, F. Chen and M. Liu, *Solid State Ionics*, 2002, **149**, 11.
13 Y. Chen, Q. Liu, Z. Yang, F. Chen and M. Han, *RSC Adv.*, 2012, **2**, 12118.
14 P. Plonczak, A. Bieberle-Hütter, M. Søgaard, T. Ryll, J. Martynczuk, P. V. Hendriksen and L. J. Gauckler, *Adv. Funct. Mater.*, 2011, **21**, 2764.
15 M. Zhi, S. Lee, N. Miller, N. H. Menzlerd and N. Wu, *Energy Environ. Sci.*, 2012, **5**, 7066.
16 A. Tarancón, S. J. Skinner, R. J. Chater, F. Hernández-Ramírez and J. A. Kilner, *J. Mater. Chem.*, 2007, **17**, 3175.
17 G. Kim, S. Wang, A. J. Jacobson, L. Reimus, P. Brodersenb and C. A. Mims, *J. Mater. Chem.*, 2007, **17**, 2500.
18 S. Hou, J. A. Alonso, S. Rajasekhara, M. J. Martínez-Lope, M. T. Fernández-Díaz and J. B. Goodenough, *Chem. Mater.*, 2010, **22**, 1071.
19 W. Zhou, Z. Shao, F. Liang, Z.-G. Chen, Z. Zhu, W. Jin and N. Xu, *J. Mater. Chem.*, 2011, **21**, 15343.
20 J. M. Porras-Vazquez, T. F. Kemp, J. V. Hanna and P. R. Slater, *J. Mater. Chem.*, 2012, **22**, 8287.
21 C. Zhang and H. Zhao, *J. Mater. Chem.*, 2012, **22**, 18387.
22 S.-E. Hou, J. A. Alonso and J. B. Goodenough, *J. Power Sources*, 2010, **195**, 280.
23 Q. Liu, X. Dong, G. Xiao, F. Zhao and F. Chen, *Adv. Mater.*, 2010, **22**, 5478.
24 B. Wei, Z. Lü, X. Huang, M. Liu, N. Li and W. Su, *J. Power Sources*, 2008, **176**, 1.
25 Y. Niu, W. Zhou, J. Sunarso, L. Ge, Z. Zhu and Z. Shao, *J. Mater. Chem.*, 2010, **20**, 9619.
26 T. Nitadori, T. Ichiki and M. Misono, *Bull. Chem. Soc. Jpn.*, 1988, **61**, 621.
27 N. A. Jordan, P. D. Battle, J. Sloan, P. Manuel and S. Kilcoyne, *J. Mater. Chem.*, 2003, **13**, 2617.
28 T. Matsui, E. Taketani, R. Sato and K. Morii, *J. Phys. D: Appl. Phys.*, 2007, **40**, 6066.
29 T. Kida, D. Takauchi, K. Watanabe, M. Yuasa, K. Shimanoe, Y. Teraoka and N. Yamazoe, *J. Electrochem. Soc.*, 2009, **156**, E187.
30 Y. Niu, W. Zhou, J. Sunarso, F. Liang, Z. Zhu and Z. Shao, *Electrochem. Commun.*, 2011, **13**, 1340.
31 H. J. V. Hook, *J. Phys. Chem.*, 1964, **68**, 3786.
32 S. Mori, *J. Am. Ceram. Soc.*, 1966, **49**, 600.
33 J. M. Gonzalez-Calbet, M. Parras, M. Vallet-Regi and J. C. Grenier, *J. Solid State Chem.*, 1990, **86**, 149.
34 M. Parras, J. M. Gonzalez-Calbet, M. Vallet-Regi and J. C. Grenier, *Solid State Ionics*, 1993, **63–65**, 714.

35 N. Hayashi, T. Yamamoto, H. Kageyama, M. Nishi, Y. Watanabe, T. Kawakami, Y. Matsushita, A. Fujimori and M. Takano, *Angew. Chem., Int. Ed.*, 2011, **50**, 12547.
36 F. Dong, D. Chen, Y. Chen, Q. Zhao and Z. Shao, *J. Mater. Chem.*, 2012, **22**, 15071.
37 T. Nagai, W. Ito and T. Sakon, *Solid State Ionics*, 2007, **177**, 3433.
38 C.-Y. Chung, Y.-H. Chang, G.-J. Chen and Y.-L. Chai, *J. Cryst. Growth*, 2005, **284**, 100.
39 H. Paik, H. Hwang, K. No, S. Kwon and D. P. Cann, *Appl. Phys. Lett.*, 2007, **90**, 042908.
40 S. Eitssayeam, U. Intatha, K. Pengpat, G. Rujijanagul, K. J. D. MacKenzie and T. Tunkasiri, *Curr. Appl. Phys.*, 2009, **9**, 993.
41 W. Zhang, L. Li and X. M. Chen, *J. Appl. Phys.*, 2009, **106**, 104108.
42 K. Watanabe, D. Takauchi, M. Yuasa, T. Kida, K. Shimanoe, Y. Teraoka and N. Yamazoe, *J. Electrochem. Soc.*, 2009, **156**, E81.
43 X. Zhu, H. Wang and W. Yang, *Solid State Ionics*, 2006, **177**, 2917.
44 X. Liu, H. Zhao, J. Yang, Y. Li, T. Chen, X. Lu, W. Ding and F. Li, *J. Membr. Sci.*, 2011, **383**, 235.
45 T. Kida, A. Yamasaki, K. Watanabe, N. Yamazoe and K. Shimanoe, *J. Solid State Chem.*, 2010, **183**, 2426.
46 X. D. Zou, S. Hovmöller, M. Parras, J. M. González-Calbet, M. Vallet-Regí and J. C. Greníer, *Acta Crystallogr., Sect. A: Found. Crystallogr.*, 1993, **49**, 27.
47 H. Falcón, J. A. Barbero, J. A. Alonso, M. J. Martínez-Lope and J. L. G. Fierro, *Chem. Mater.*, 2002, **14**, 2325.
48 P. G. Radaelli and S.-W. Cheong, *Phys. Rev. B: Condens. Matter*, 2002, **66**, 094408.
49 M. Katsuki, S. Wang, M. Dokiya and T. Hashimoto, *Solid State Ionics*, 2003, **156**, 453.
50 Y. Niu, J. Sunarso, F. Liang, W. Zhou, Z. Zhu and Z. Shao, *J. Electrochem. Soc.*, 2011, **158**, B132.
51 D. Chen and Z. Shao, *Int. J. Hydrogen Energy*, 2011, **36**, 6948.
52 S. B. Adler, J. A. Lane and B. C. H. Steele, *J. Electrochem. Soc.*, 1996, **143**, 3554.
53 Y. Lu, C. Kreller and S. B. Adler, *J. Electrochem. Soc.*, 2009, **156**, B513.
54 J. Piao, K. Sun, N. Zhang, X. Chen, S. Xu and D. Zhou, *J. Power Sources*, 2007, **172**, 633.
55 S. Jiang, W. Zhou, Y. Niu, Z. Zhu and Z. Shao, *ChemSusChem*, 2012, **5**, 2023.
56 Q. Zhou, L. Xu, Y. Guo, D. Jia, Y. Li and W. C. J. Wei, *Int. J. Hydrogen Energy*, 2012, **37**, 11963.
57 S. Wang, *Ionics*, 2012, **18**, 777.
58 D. Chen, F. Wang, H. Shi, R. Ran and Z. Shao, *Electrochim. Acta*, 2012, **78**, 466.
59 W. Zhou, Z. Shao, R. Ran and R. Cai, *Electrochem. Commun.*, 2008, **10**, 1647.
60 F. Dong, D. Chen, R. Ran, H. Park, C. Kwak and Z. Shao, *Int. J. Hydrogen Energy*, 2012, **37**, 4377.